Real-time Subsynchronous Control Interaction Monitoring Using Improved Intrinsic Time-scale Decomposition

Yang Wang, Hanlu Yang, Xiaorong Xie, Xiaomei Yang, and Guanrun Chen

***Abstract*—In recent years, subsynchronous control interaction (SSCI) has frequently taken place in renewable-connected power systems. To counter this issue, utilities have been seeking tools for fast and accurate identification of SSCI events. The main challenges of SSCI monitoring are the time-varying nature and uncertain modes of SSCI events. Accordingly, this paper presents a simple but effective method that takes advantage of intrinsic time-scale decomposition (ITD). The main purpose is to improve the accuracy and robustness of ITD by incorporating the least-squares method. Results show that the proposed method strikes a good balance between dynamic performance and estimation accuracy. More importantly, the method does not require any prior information, and its performance is therefore not affected by the frequency constitution of the SSCI. Comprehensive comparative studies are conducted to demonstrate the usefulness of the method through synthetic signals, electromagnetic temporary program (EMTP) simulations, and field-recorded SSCI data. Finally, real-time simulation tests are conducted to show the feasibility of the method for real-time monitoring.**

***Index Terms*—Subsynchronous control interaction (SSCI), intrinsic time-scale decomposition (ITD), wind power system, real-time monitoring.**

I. Introduction

An undesirable outcome of the surging application of wind generators is the increased risk of subsynchronous control interaction (SSCI) [1]-[4]. In recent years, SSCI incidents have been observed in several real-life wind farms (WFs) such as WFs under the Electric Reliability Council of Texas (ERCOT), USA, and those in Hami, China [5]. To deal with this issue, utilities have been seeking effective tools for fast and accurate identification of SSCI events [6]. The identified SSCI parameters are crucial for tripping critical wind generators, replicating SSCI events, and supporting the design of countermeasures [7], [8].

Existing power system monitoring devices such as phasor measurement units are designed for fundamental phasors at 50 Hz or 60 Hz. Although it has been recently reported that SSCI parameters can be identified from synchrophasors [8]-[12], their precision is strongly affected by the reporting rate and low-pass filter [12]. Thus, installing waveform-based devices that are custom-designed for SSCI monitoring is preferable. This type of project has been initiated in Xinjiang, China.

Considering the time-varying and frequency-coupling nature of SSCI [5], the algorithm used for SSCI monitoring should have good dynamic performance and robustness against the frequency constitution. This poses a challenge in terms of selecting algorithms. For example, discrete Fourier transform (DFT) methods can implement spectral analysis of signals with multiple frequency components, but the high accuracy of DFT methods requires a long window, which sacrifices dynamic performance. Moreover, spectrum leakage and picket-fence effect lead to errors in estimation results [13]. Traditional mode identification methods such as Prony [14], eigensystem realization algorithm (ERA) [15], matrix pencil method (MPM) [16], and total least squares-estimation of signal parameters via rotational invariance technique (TLS-ESPRIT) [17] have been widely used for oscillation monitoring. However, the number of modes must be carefully selected, which can be a challenge for SSCI. In addition, the computation burden of these approaches may be too large in practical engineering applications, as a large number of samples are generally needed. Time-domain methods such as recursive-least-squares-based methods [18], [19], Kalman-filter-based methods [20], and waveform-envelop-based methods [21], [22] are expected to have good dynamic performance. Yet, these methods require that either the magnitude of the fundamental frequency current be constant or that the prior knowledge of the SSCI frequency exist, which is not always available. In [23], synchronized waveform data collected at both sides of the series-compensated line are used to identify SSCI. Although this method is innovative, it is applicable only in cases in which synchronized waveform measurement units and series capacitors are available. In addition, some advanced algorithms have been proposed in recent years. For

Manuscript received: July 11, 2021; revised: January 5, 2022; accepted: March 5, 2022. Date of CrossCheck: March 5, 2022. Date of online publication: May 13, 2022.

This work was supported in part by the National Natural Science Foundation of China (No. 51907133) and in part by the Fundamental Research Funds for the Central Universities (No. YJ201911).

Y. Wang, H. Yang, X. Yang (corresponding author), and G. Chen are with the College of Electrical Engineering, Sichuan University, Chengdu, China (e-mail: fwang@scu. edu. cn; 18328036566@163. com; yangxiaomei@scu. edu. cn; 2051935335@qq.com).

X. Xie is with the Department of Electrical Engineering, Tsinghua University, Beijing, China. (e-mail: xiexr@tsinghua.edu.cn).

DOI: 10.35833/MPCE.2021.000464

example, in [24], a bandpass digital-filter-based method is proposed for interharmonic parameter estimation. It uses 50-cycle DFT to precompute interharmonic frequencies and then designs filters. This type of extremely long data window leads to long latency and is thus a major issue. In [25], an improved iterative Taylor-Fourier multifrequency-model based method is proposed, but its performance has been found to be vulnerable to wideband noise, fundamental frequency deviation, and interharmonic frequency ramps. In addition, these advanced algorithms are generally very complicated and thus are difficult to implement in practice.

This paper proposes a simple but efficient method for fast and accurate identification of SSCI events, which is particularly suitable for real-time monitoring. The primary purpose of this paper is to take advantage of the intrinsic time-scale decomposition (ITD) algorithm. Originally, ITD extracted the oscillation components of the signal by fitting the upper and lower enveloping lines of the measured signal. ITD has many distinct advantages such as superior dynamic performance and a lack of prior information. However, as a time-domain algorithm, ITD is vulnerable to noise and cannot monitor oscillation energy continuously. To address this issue, this paper improves the ITD algorithm by incorporating the least-squares method. Consequently, a two-stage SSCI identification process is established that retains the dynamic performance of the ITD and is capable of continuously tracking the SSCI parameters. Comparative studies are conducted to verify the effectiveness and robustness of the proposed method using synthetic signals, real-time simulation tests, and field data.

The remainder of this paper is organized as follows. Section II explains the proposed method including the ITD algorithm and SSCI monitoring strategy. Section III describes the simulation verifications of the proposed method using synthetic signals and electromagnetic temporary program (EMTP) simulations. The section also describes a comparison with conventional methods to demonstrate the merits of the proposed method. Section IV describes the field data verification to evaluate the performance of the proposed method for real-life SSCI events. Section V presents a real-time simulation validation to demonstrate the practical implementation of the proposed method. Finally, conclusions are given in Section VI.

II. Proposed Method

In this section, we introduce the original ITD algorithm. The challenges for SSCI monitoring are discussed along with the proposed method. A strategy for SSCI monitoring is then presented.

A. ITD Algorithm

ITD can adaptively decompose a signal into multiple oscillation components. The extraction principle is to fit the envelope of the original signal using linear interpolation and to define the key points of the oscillation components using the upper and lower envelopes near the signal extrema. The low-frequency components can then be obtained by interpolating the key points, and the high-frequency components can be determined by subtracting the low-frequency components from the original signal. Additional details of the ITD algorithm are described as follows [26].

As shown in Fig. 1, for an original signal X_t ($t \geq 0$), an extraction operator $\mathcal{L}$ is defined to decompose X_t into low- and high-frequency components L_t and H_t, respectively, and then X_t can be expressed by:

$$X_t = \mathcal{L}X_t + (1-\mathcal{L})X_t = L_t + H_t \tag{1}$$

where $L_t = \mathcal{L}X_t$; and $H_t = (1-\mathcal{L})X_t$.

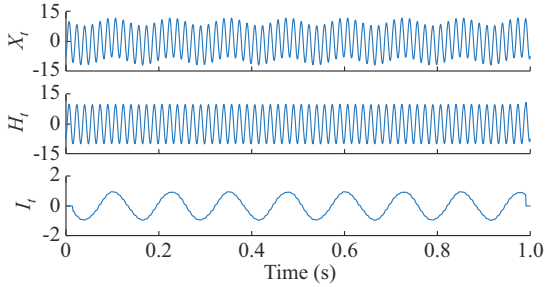

Fig. 1. Decomposition process of ITD algorithm.

Accordingly, the ITD algorithm must determine the extreme points X_k within the specified time interval and the corresponding occurrence time instant τ_k ($k \in N^+$), as shown in Fig. 2. Suppose that L_t and H_t are given over $[0, \tau_k]$ and that X_t is defined in $[0, \tau_{k+2}]$. To extract the low-frequency oscillatory component, the extraction operator $\mathcal{L}$ on contiguous extrema interval $[\tau_k, \tau_{k+1}]$ is defined as:

$$\mathcal{L}X_t = L_t = L_k + \frac{L_{k+1}-L_k}{X_{k+1}-X_k}(X_t - X_k) \quad t \in (\tau_k, \tau_{k+1}) \tag{2}$$

where $L_k = L(\tau_k)$ and L_{k+1} correspond to the points in the low-frequency oscillation component, with L_{k+1} given by:

$$L_{k+1} = 0.5\left[X_k + \frac{\tau_{k+1}-\tau_k}{\tau_{k+2}-\tau_k}(X_{k+2}-X_k)\right] + 0.5X_{k+1} \tag{3}$$

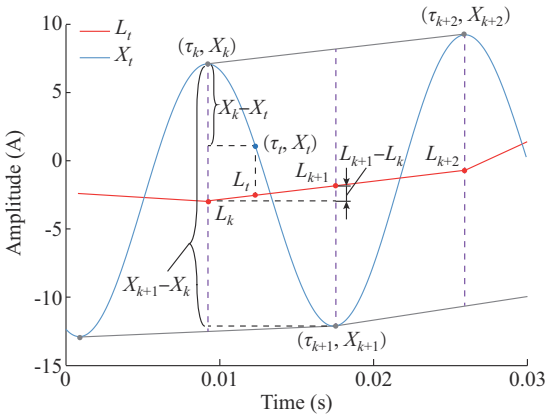

Fig. 2. Principle of ITD algorithm.

Following the first decomposition of the original signal X_t, a high-frequency oscillation signal H_t is obtained by:

$$H_t = X_t - L_t = (1-\mathcal{L})X_t = \mathcal{H}X_t \tag{4}$$

where $\mathcal{H}$ is the extraction operator of the high-frequency component.

In addition, take L_t in (2) as the input signal, and repeat

the aforementioned decomposition process until the termination condition is satisfied. Eventually, after p iterations, the original signal X_t is decomposed as:

$$X_t=\mathcal{H}X_t+\mathcal{L}X_t=\mathcal{H}X_t+(\mathcal{H}+\mathcal{L})\mathcal{L}X_t=$$
$$[\mathcal{H}(1+\mathcal{L})+\mathcal{L}^2]X_t=\left(\mathcal{H}\sum_{k=0}^{p-1}\mathcal{L}^k+\mathcal{L}^p\right)X_t=$$
$$H_t^1+H_t^2+\ldots+H_t^p+L_t^p \tag{5}$$

where H_t^k ($k=1,2,\ldots,p$) is the k^{th} high-frequency component; and L_t^p is the extracted lowest-frequency component. The termination condition is set according to the requirements (e.g., when the energy of L_t^p is less than 2% of X_t).

B. Two-stage ITD Algrithm

As shown in the previous subsection, the ITD algorithm is simple and does not require any prior mode information. However, when applied to SSCI monitoring, it faces the following several challenges.

1) The amplitude of oscillation is determined by the peak points in the extracted waveform, i. e., L_t in Fig. 3. This means that the oscillation energy can be assessed only when a peak is detected, which means that monitoring is "discontinuous".

2) The extracted waveform L_t is determined and fitted using the extreme points of the original signal. In some cases, the fitness error may be large. For example, in Fig. 3, the fitted peak is at point *K*, whereas the real peak is at point *P*.

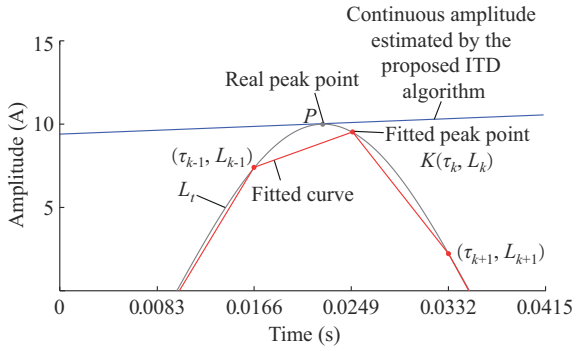

Fig. 3. Explanation of amplitude fitness error.

3) The ITD experiences difficulty in detecting supersynchronous oscillation, as the component in this frequency range (i.e., $f_0<f_{sup}<2f_0$, where f_{sup} is the frequency of supersynchronous oscillation and f_0 is the fundamental frequency) has a smaller effect on the extreme points of waveforms at the fundamental frequency, i.e., 50 Hz or 60 Hz.

4) ITD is vulnerable to noise because the fitted curve is determined by the extrema of the sampled signal. Figure 4 shows the fitting performances of the proposed method with and without 35 dB noise, where y_{n1} represents the reference curve, and y_{n2} and y_{n3} represent the ITD fitted curves without and with 35 dB noise, respectively. It can be observed that the fitted amplitude is inaccurate under the noise condition.

To overcome the aforementioned shortcomings, this paper proposes a two-stage ITD algorithm that incorporates the least-squares method.

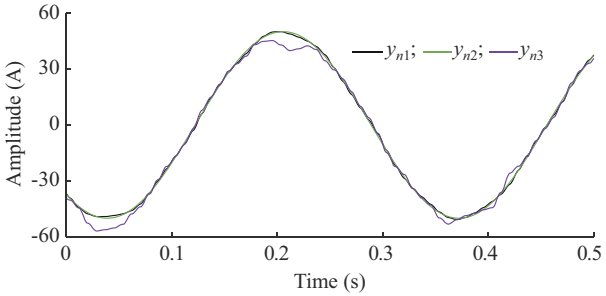

Fig. 4. Fitting performance of proposed method with and without 35 dB noise.

1) Stage 1: Frequency Estimation

To estimate the frequency of the oscillation component, the current signal rather than the voltage is used as the oscillation, which is generally more obvious in the current. According to (3), the key points L_k of the oscillation component are defined by the extreme points X_k in the original signal. For two consecutive points that satisfy (6), a zero-crossing point (t_z, L_z), $t_z\in[\tau_k,\tau_{k+1}]$ must exist, and the corresponding X_z can be obtained using (7).

$$L_{k+1}L_k<0 \tag{6}$$

$$L_z=L_k+\frac{L_{k+1}-L_k}{X_{k+1}-X_k}(X_z-X_k)=0 \tag{7}$$

As the original curve X_z between two extreme points is monotonic, the abscissa of point X_z can be obtained, which is the abscissa of the zero-crossing point t_z.

Based on the distance between two adjacent zero-crossing points (L_{z-1}, L_z), the frequency of the oscillation component can be determined by:

$$f_{\text{sub}}=1/[2dt_1\cdot(t_z-t_{z-1})] \tag{8}$$

where f_{sub} is the instantaneous frequency of the subsynchronous component, which is updated whenever a zero-crossing point appears; and dt_1 is the sampling time of the original signal.

To estimate the fundamental frequency f_0, the voltage signal rather than the current is used because the subsynchronous component is limited to the voltage even if oscillation occurs. The fundamental frequency f_0 can be estimated as:

$$f_0=1/[2dt_1\cdot(tv_i-tv_{i-1})] \tag{9}$$

where tv_i and tv_{i-1} are the newly updated locations of the two consecutive zero-crossing points in the voltage signal.

2) Stage 2: Amplitude Estimation

To handle the challenges of estimating amplitude, the least-squares method is adopted in the second stage. Based on the estimated frequencies of the subsynchronous and fundamental components in the first stage, i. e., f_{sub} and f_0, we can construct the eigenvalue vector $\boldsymbol{\lambda}$ of the sampled signal as:

$$\boldsymbol{\lambda}=[\lambda_1\ \lambda_2\ \ldots\ \lambda_{2i}]^{\text{T}}=\left[\text{e}^{\sigma_1\pm\text{j}\omega_1}\ \text{e}^{\sigma_2\pm\text{j}\omega_2}\ \ldots\ \text{e}^{\sigma_i\pm\text{j}\omega_i}\right]^{\text{T}}\quad i=1,2,\ldots,q \tag{10}$$

$$\omega_i=2\pi f_i \tag{11}$$

where σ_i and f_i are the damping factor and frequency of the i^{th} component in the measured signal, respectively. In this pa-

per, q equals 3 for three modes, i.e., the fundamental, subsynchronous, and supersynchronous components. The supersynchronous component is derived from the frequency coupling effect [5] and can be determined by the former two components as:

$$f_{\text{sup}} = 2f_0 - f_{\text{sub}} \tag{12}$$

Since $\sigma_i \ll \omega_i$, the contribution of damping to the eigenvalues can be ignored, leading to $\lambda_{2i-1} = e^{-j\omega_i}$ and $\lambda_{2i} = e^{+j\omega_i}$. Then, the Vandermonde matrix $\boldsymbol{A} \in \mathrm{C}^{m \times 2q}$ is constituted by the eigenvalues $\boldsymbol{\lambda}$ as:

$$\boldsymbol{A} = \begin{bmatrix} \lambda_1^0 & \lambda_2^0 & \cdots & \lambda_{2q}^0 \\ \lambda_1^1 & \lambda_2^1 & \cdots & \lambda_{2q}^1 \\ \vdots & \vdots & & \vdots \\ \lambda_1^{m-1} & \lambda_2^{m-1} & \cdots & \lambda_{2q}^{m-1} \end{bmatrix} \tag{13}$$

where m is the sample number of the signal. In this paper, the signal refers to the sampled current and voltage, i.e., $\boldsymbol{Y}_I \in \mathbf{R}^{m \times 1}$ and $\boldsymbol{Y}_V \in \mathbf{R}^{m \times 1}$, which are expressed as:

$$\boldsymbol{Y}_I = [y_{I1}\ y_{I2}\ \cdots\ y_{Im}]^{\mathrm{T}} \tag{14}$$

$$\boldsymbol{Y}_V = [y_{V1}\ y_{V2}\ \cdots\ y_{Vm}]^{\mathrm{T}} \tag{15}$$

Based on the Euler equation, $\boldsymbol{Y}_I = \boldsymbol{A}\boldsymbol{C}_I$ and $\boldsymbol{Y}_V = \boldsymbol{A}\boldsymbol{C}_V$ [12], where $\boldsymbol{C}_I$ and $\boldsymbol{C}_V$ are the phasors of each mode for the current and voltage signals, respectively. Using the least-squares method, $\boldsymbol{C}_I$ and $\boldsymbol{C}_V$ can be obtained as:

$$\boldsymbol{C}_I = (\boldsymbol{A}^{\mathrm{T}}\boldsymbol{A})^{-1}\boldsymbol{A}^{\mathrm{T}}\boldsymbol{Y}_I \tag{16}$$

$$\boldsymbol{C}_V = (\boldsymbol{A}^{\mathrm{T}}\boldsymbol{A})^{-1}\boldsymbol{A}^{\mathrm{T}}\boldsymbol{Y}_V \tag{17}$$

The number of data points used for the voltage and current phasor estimations and the corresponding mean of relative errors are listed in Table I. Table I shows that when more data points are used, the relative errors are lower. However, the dynamic performance is degraded and the computational burden is higher. Our experiments have shown that 10 points strike a good balance between dynamic performance and estimation accuracy, as the improvement in relative errors from 10 to 20 points is not significant. Thus, 10 data points are used in this paper. Using the least-squares method, we could continuously calculate the phasor of the SSCI. More importantly, both the subsynchronous and supersynchronous components could be extracted reliably with less sensitivity to noise. A comparison between the original and proposed ITD algorithms is presented in Table II.

TABLE I
NUMBER OF DATA POINTS USED FOR VOLTAGE AND CURRENT PHASOR ESTIMATIONS AND CORRESPONDING MEAN OF RELATIVE ERRORS

Number of data points	Mean of relative errors (%)
5	5.40
8	1.27
10	1.01
20	0.98
40	0.96

C. Strategy for SSCI Monitoring

The SSCI monitoring device is designed to include three modules: signal preprocessing, monitoring, and decision.

TABLE II
COMPARISON BETWEEN ORIGINAL AND PROPOSED ITD ALGORITHM

ITD	Continuity of estimation	Amplitude fitness error	Calculation burden	Anti-noise performance
Original	No	Large	Small	Week
Proposed	Yes	Small	Relatively larger	Strong

1) Signal Preprocessing Module

The objective of this module is to filter out undesirable noise in the measured current and voltage signals. An 8-order lowpass finite impulse response (FIR) filter is designed for this purpose. The filter is designed using a Hamming window with a cutoff frequency of 120 Hz.

2) Monitoring Module

In the monitoring block, the proposed ITD algorithm is applied to extract the oscillation components. The frequency is updated once a zero-crossing point is detected according to (8), (9), and (12), whereas the phasor is calculated continuously using 10 data points according to (16) and (17). To guarantee real-time detection, the ITD algorithm is executed whenever new sample data are received.

3) Decision Module

The detection of an SSCI event is confirmed if the following three requirements are met. Subsequently, the device sends an early-warning or tripping signal based on user needs.

1) Frequency range: the frequency of the subsynchronous component should fall within the range of [5, 55]Hz in a 60 Hz system. Otherwise, it is not defined as SSCI [15].

2) Oscillation magnitude: a threshold of the oscillation magnitude must be defined to strike a balance between reliability and speed of detection. In this paper, 10% of the amplitude of the fundamental component is selected as the threshold. As with any other protection function, the threshold can be adjusted according to the needs of utility.

3) The minimum detection time: to avoid improper operation due to unexpected disturbances, it is suggested that a warning signal be sent after oscillations are sustained over a certain period. A minimum detection time of 50 ms is set for this purpose and can be adjusted according to the needs of utility.

III. SIMULATION VERIFICATIONS

The proposed method is evaluated using synthetic signals and EMTP simulations. Its performance is compared with industry-preferred algorithms, including Prony, ERA, MPM, and TLS-ESPRIT. The sampling rate is set to be 1000 Hz for fast detection of the oscillation, and a 40 ms window is adopted for all algorithms to achieve a fair comparison. It is worth mentioning that in the first stage, the proposed method continues to find the zero-crossing point to obtain the latest frequency. Thus, no data window is required. In the second stage, 10 data points in a 40 ms window are used for the least-squares method. A length of 40 ms is determined through trial and error to strike a balance between estimation accuracy and dynamic performance. The setting of each method remains the same as that in the following verifications.

A. Synthetic Signals

The synthetic data Y_0 is modeled as the superimposition of fundamental, subsynchronous, and supersynchronous components and is given by:

$$Y_0 = A_0\cos(2\pi f_0 t+\varphi_1)+A_{\text{sub}}\mathrm{e}^{\sigma t}\cos(2\pi f_{\text{sub}}t+\varphi_2)+ A_{\text{sup}}\mathrm{e}^{\sigma t}\cos(2\pi f_{\text{sup}}t+\varphi_3) \quad (18)$$

where (A_0,φ_1), $(A_{\text{sub}},\varphi_2)$, and $(A_{\text{sup}},\varphi_3)$ are the amplitudes and initial phases of the fundamental, subsynchronous, and supersynchronous components, respectively; $f_0=60$ Hz; $A_{\text{sub}}=A_{\text{sup}}=A_0\times 10\%$; and the damping factor σ of the subsynchronous and supersynchronous components is set to be 0.2.

1) Impact of Harmonic Distortions

To verify the influence of high-order harmonics on the proposed method, the mathematical model given in (19) is considered, where the amplitude of the SSCI is 10% of the fundamental component, and the amplitudes of the 3rd, 5th, and 7th harmonics are 5% of the fundamental component.

$$\begin{aligned} y_{TS} = {} & 30\cos(2\pi\times 60+30)+3\cos(2\pi\times 8+20)+ \\ & 3\cos(2\pi\times(2\times 60-8)+10)+1.5\cos(2\pi\times 60\times 3+30)+ \\ & 1.5\cos(2\pi\times 60\times 5+20)+1.5\cos(2\pi\times 60\times 7+10) \end{aligned} \quad (19)$$

Figure 5 shows the performance of the proposed method with high-order harmonics, where y_{TS} is the test signal; and $y_{TS,fil}$ is the signal after processing by the low-pass filter. As shown in Fig. 5, the proposed method performs satisfactorily under harmonic conditions because of the well-designed low-pass filters.

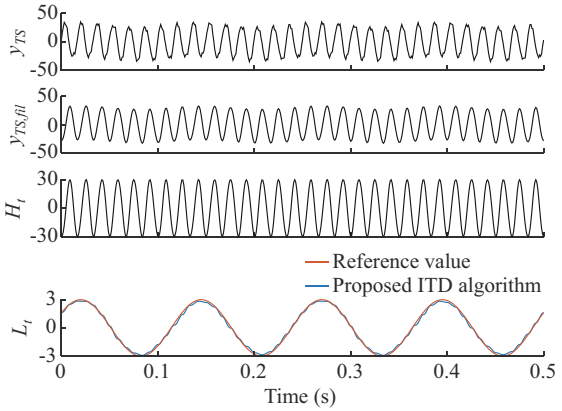

Fig. 5. Performance of proposed method with high-order harmonics.

2) Noisy Conditions

A general signal-to-noise ratio (SNR) sampled at the monitoring devices is approximately 45 dB [12]. Thus, white noise with SNR = 35 dB is added to signal Y_1.

$$\begin{aligned} Y_1 = {} & 300\cos(2\pi\times 60t+10°)+30\cos(2\pi\times 13t+20°)+ \\ & 30\cos(2\pi\times(120-13)t+30°) \end{aligned} \quad (20)$$

Figure 6(a) and (c) shows the estimated frequency and magnitude, respectively, with a window length of 40 ms. The corresponding mean and variance of the relative errors for five algorithms with SNR of 35 dB in a 40 ms window are listed in Table III. Due to limited space, only the results of subsynchronous component are presented, where the findings for the supersynchronous component are similar. Compared with conventional algorithms, the performance of the proposed ITD algorithm is found to be more robust under noisy conditions. In addition, a moving window of 100 ms is used for all algorithms, and the results are shown in Fig. 6(b) and (d). Comparing Fig. 6(a) and (c), we can conclude that a longer window helps to enhance the performance of all algorithms, with the proposed ITD algorithm still showing the best performance. However, it should be noted that a shorter window generally indicates better dynamic performance.

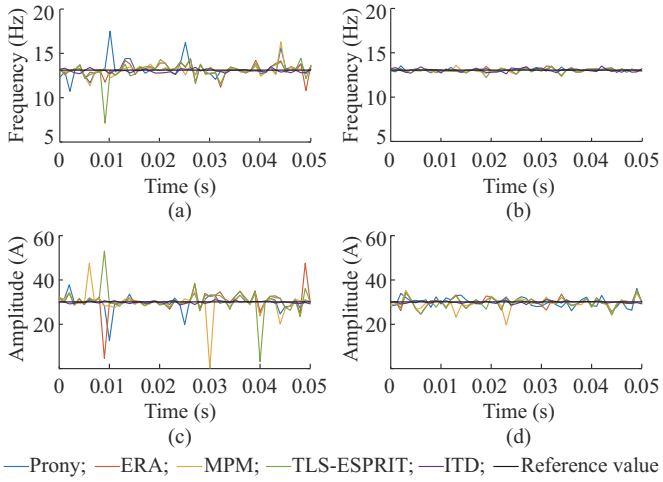

Fig. 6. Estimation results of five algorithms under white noise with SNR of 35 dB. (a) Frequency with a 40 ms window. (b) Frequency with a 100 ms window. (c) Amplitude with a 40 ms window. (d) Amplitude with a 100 ms window.

TABLE III
MEAN AND VARIANCE OF RELATIVE ERRORS FOR FIVE ALGORITHMS WITH SNR OF 35 DB IN A 40 MS WINDOW

Algorithm	Frequency (mean ± variance) (%)	Amplitude (mean ± variance) (%)
Prony	2.94 ± 0.16	7.10 ± 0.91
ERA	6.02 ± 1.56	9.32 ± 2.11
MPM	5.84 ± 2.23	10.26 ± 4.29
TLS-ESPRIT	4.25 ± 0.36	8.97 ± 1.67
ITD	1.26 ± 0.02	1.28 ± 0.03

In the aforementioned studies, the number of modes of conventional methods is carefully selected through trial and error to achieve a result that is the closest to the reference value. This mode selection, however, cannot be performed in practice. Although some automatic mode-selection methods have been proposed [27], their performance cannot be guaranteed under noisy conditions. When the mode is improperly selected, the results will degrade significantly. For instance, if the number of modes is fixed at 3, the results of the five algorithms are shown in Fig. 7, which shows that the conventional algorithms perform poorly.

3) Dynamic Conditions

The frequency and amplitude of SSCI components are usually time-variant because of various highly uncertain factors, including changing network topologies and the stochastic nature of wind resources. Thus, the good dynamic performance

of the algorithm is important for SSCI monitoring. In this experiment, variations in the frequency and magnitude of the fundamental and SSCI components were considered.

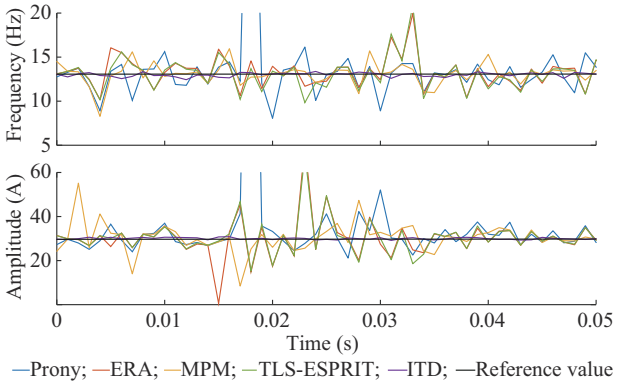

Fig. 7. Estimation results of five algorithms under white noise with SNR of 35 dB and modes of conventional algorithms fixed at 3.

First, based on the fact that the frequency of the fundamental component varies with time, the synthetic signal Y_2 is given as:

$$Y_2 = 100\cos(2\pi\times(60+t)t+10°)+10e^{0.2t}\cos(2\pi\times 13t+20°)+ 10e^{0.2t}\cos(2\pi\times(120-13)t+30°) \quad (21)$$

The results shown in Fig. 8 reveal that the ITD performs best under a variation in the fundamental frequency. This is because the change in the fundamental frequency affects the estimation of the eigenvalue more significantly with the conventional algorithms than with the proposed ITD algorithm.

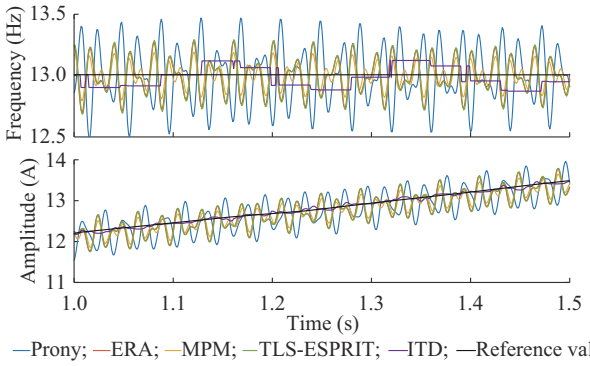

Fig. 8. Estimation results of five algorithms under dynamic f_0.

Similarly, to simulate the frequency variation of the SSCI component, a synthetic signal Y_3 was generated as:

$$Y_3 = 100\cos(2\pi\times 60t+10°)+10e^{0.2t}\cos(2\pi\times(13+t)t+20°)+ 10e^{0.2t}\cos(2\pi\times(120-13-t)t+30°) \quad (22)$$

The estimation results for the five algorithms under dynamic f_{ssr} are shown in Fig. 9. In this case, all algorithms perform well because of proper mode selection.

When the step change in the amplitude of the fundamental component is considered, the synthetic signal Y_4 is given by:

$$Y_4 = 100[1-0.1\varepsilon(t-0.02)]\cos(2\pi\times 60t+10°)+ 10e^{0.2t}\cos(2\pi\times 13t+20°)+10e^{0.2t}\cos(2\pi\times(120-13)t+30°) \quad (23)$$

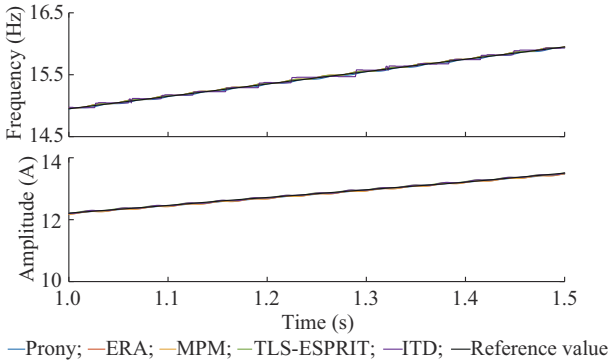

Fig. 9. Estimation results of five algorithms under dynamic f_{ssr}.

Similarly, to simulate the step change in the amplitudes of the SSCI components, the synthetic signal Y_5 is given by:

$$Y_5 = 100\cos(2\pi\times 60t+10°)+ 10e^{0.2t}[1-0.1\varepsilon(t-0.02)]\cos(2\pi\times 13t+20°)+ 10e^{0.2t}[1-0.1\varepsilon(t-0.02)]\cos(2\pi\times 107t+30°) \quad (24)$$

The paired subfigures of Fig. 10(a), (c) and (b), (d) show the estimated results of the SSCI components for Y_4 and Y_5, respectively. Compared with the other four algorithms, the proposed ITD algorithm performs best under step-change conditions. This observation is confirmed by the mean and variance of the relative errors between the estimated and real values, as shown in Table IV.

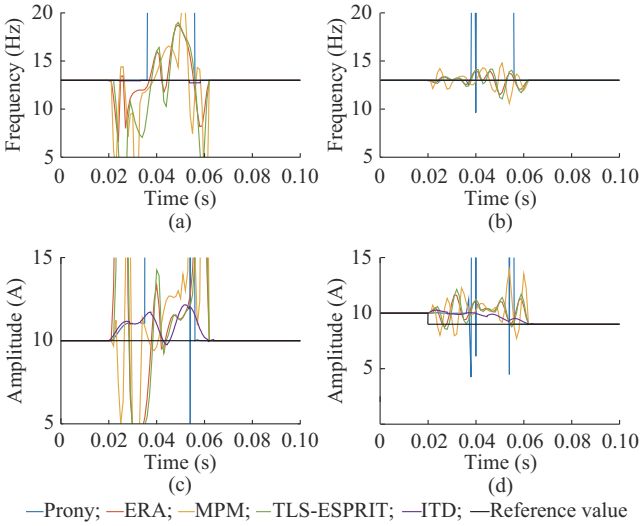

Fig. 10. Frequency and amplitude tracking performance of five algorithms under fundamental and subsynchronous amplitude step-change conditions. (a) Frequency with step change of fundamental component. (b) Frequency with step change of SSCI component. (c) Amplitude with step change of fundamental component. (d) Amplitude with step change of SSCI component.

The superior performance of the proposed ITD algorithm is attributed to the separate estimation of the frequency and amplitude. In general, even under a step change of amplitudes, the proposed ITD algorithm could still accurately determine the frequency of the SSCI, which in turn benefits the fitness of the amplitude.

TABLE IV
MEAN AND VARIANCE OF RELATIVE ERRORS OF FIVE ALGORITHMS UNDER AMPLITUDE STEP-CHANGE CONDITIONS

Algorithm	Frequency of Y_4 (mean ± variance) (%)	Amplitude of Y_4 (mean ± variance) (%)	Frequency of Y_5 (mean ± variance) (%)	Amplitude of Y_5 (mean ± variance) (%)
Prony	89.97 ± 323.93	278.44 ± 2994.46	90.64 ± 328.66	259.25 ± 2663.11
ERA	8.44 ± 2.74	49.27 ± 230.92	1.78 ± 0.05	5.66 ± 1.14
MPM	10.48 ± 5.07	33.58 ± 101.50	1.74 ± 0.11	6.43 ± 1.56
TLS-ESPRIT	12.36 ± 5.86	39.64 ± 87.96	1.37 ± 0.08	5.69 ± 1.21
ITD	0.15 ± 0.00	8.75 ± 2.26	0.00 ± 0.00	3.06 ± 0.54

B. EMTP Simulations

An ERCOT wind power system is used to test the proposed method [28]. As shown in Fig. 11, the system is modeled on the PSCAD/EMTDC platform for electromagnetic transient simulations. The system contains several WFs based on doubly-fed induction generators, and a series capacitor is placed between buses 5 and 6.

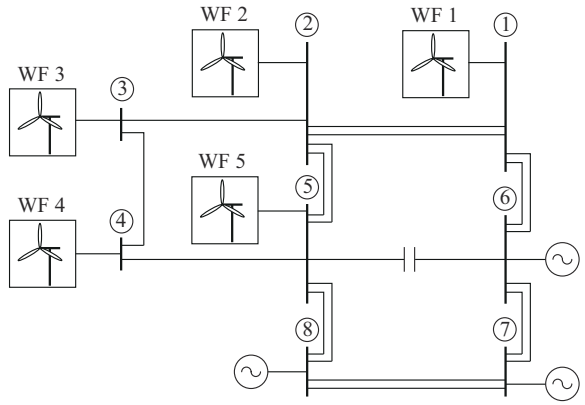

Fig. 11. Single-line diagram of ERCOT test system.

A detailed description of this system can be found in [28]. In this simulation, the minimum detection time module is disabled to observe the tracking abilities of the five algorithms.

The reference values in Fig. 12 are obtained by a high-order low-pass filter, which can hardly be used in real time but has satisfactory performance in offline analysis.

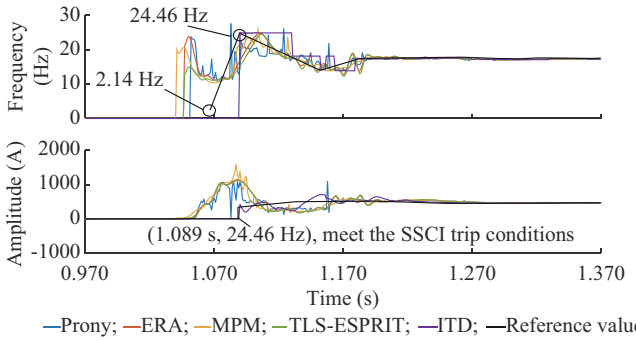

Fig. 12. Frequency and amplitude tracking performances of five algorithms in SSCI event.

In this case, a three-phase fault occurs on one line between buses 5 and 8 at 1 s, which is cleared after 100 ms (six cycles). The simulation results are shown in Fig. 13, where a large transient is induced by the three-phase fault, and the SSCI commences immediately after the fault is cleared. Figure 12 and Table V show that all algorithms detect the SSCI component before the fault is cleared because there is indeed a transient component with a frequency of 24.46 Hz. However, only the proposed ITD algorithm accurately captures the frequency of this transient, while the other algorithms detects a transient with an incorrect frequency even before this transient appears. Thus, the proposed ITD algorithm is more reliable than the other algorithms under dynamic conditions.

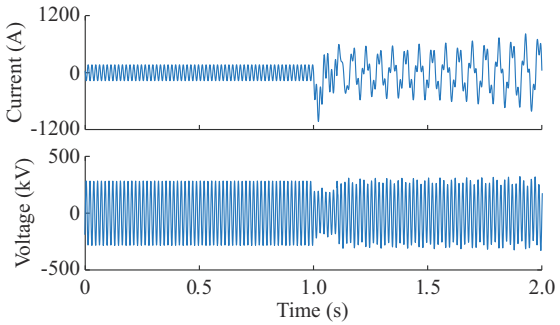

Fig. 13. Current and voltage waveforms of SSCI event in an EMTP simulation.

TABLE V
TIME FOR SENDING A WARNING SIGNAL WITH FIVE ALGORITHMS

Algorithm	Time (s)
Prony	1.051
ERA	1.046
MPM	1.040
TLS-ESPRIT	1.046
ITD	1.089

IV. FIELD DATA VERIFICATION

To further validate the real-life performance of the proposed method, we have collected the voltage and current waveforms measured during the Guyuan and Hami SSCI incidents in China, as shown in Fig. 14(a), (c) and (b), (d), respectively. The corresponding results of the five algorithms are shown in Figs. 15(a)-(c) and 16(a)-(c), respectively. The reference value is again obtained using a well-designed low-pass filter.

Compared with the conventional algorithms, the proposed method is closer to the reference value, as shown in Figs. 15 and 16. Similar to the previous verifications, the mode order of the conventional algorithms is determined through trial and error to achieve the best performance. Their performances degrade significantly when the order is not properly selected. A comparison of different rows in Table VI reveals that a 40 ms data window is sufficient for the proposed ITD algorithm. This indicates that a short window can be used in practice to achieve good dynamic performance.

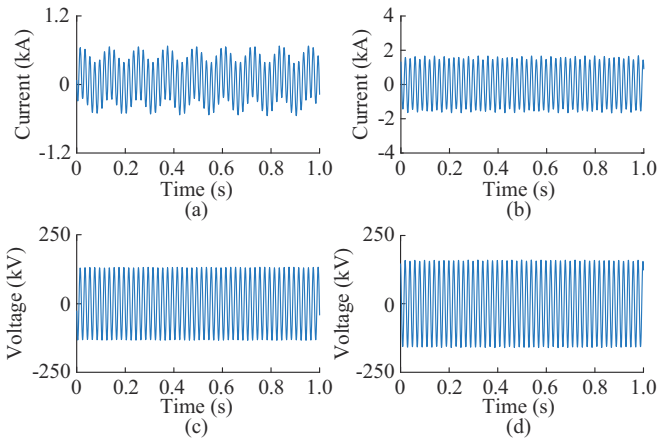

Fig. 14. Current and voltage waveform of field data in Guyuan and Hami, China. (a) Current in Guyuan. (b) Current in Hami. (c) Voltage in Guyuan. (d) Voltage in Hami.

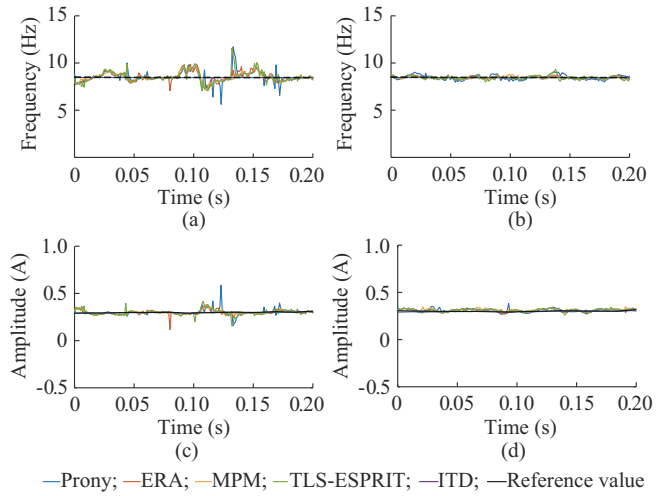

Fig. 15. Frequency and amplitude estimation results of five algorithms of field data in Guyuan. (a) Frequency with a 40 ms window. (b) Frequency with a 100 ms window. (c) Amplitude with a 40 ms window. (d) Amplitude with a 100 ms window.

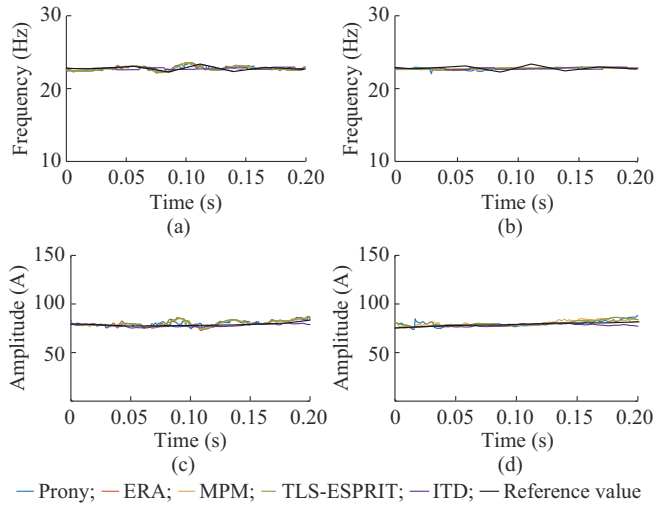

Fig. 16. Frequency and amplitude estimation results of five algorithms of field data in Hami. (a) Frequency with a 40 ms window. (b) Frequency with a 100 ms window. (c) Amplitude with a 40 ms window. (d) Amplitude with a 100 ms window.

V. Real-time Simulation Validation

To verify the performance of the proposed ITD algorithm for real-time SSCI monitoring in practical engineering applications, a real-time simulation test is conducted [29]. An algorithm complexity analysis and real-time simulation tests are presented in this section.

A. Algorithm Complexity Analysis

The time complexity reflects the computation complexity of the algorithm. This is the primary computation burden of the algorithm in the controller and can be described by:

$$T_n = O(n) \tag{25}$$

where n is the number of instructions to run the algorithm; and O is the symbol of the time complexity. The bigger n is, the larger the computation burden will be. The time complexity of each algorithm can be represented by its dominant module. Therefore, the time complexities of the different algorithms have been evaluated, with the results presented in Table VII. The table shows that the proposed ITD algorithm possesses the lowest computational burden, making it more suitable for practical engineering applications.

B. Real-time Simulation Test

As shown in Appendix A Fig. A1, the wind power system shown in Fig. 11 is modeled using the real-time simulation device Typhoon HIL 402 with a step of 20 μs, and the simulated analog voltage and current signals are fed into the DSP 28335 control board in which the proposed ITD algorithm is embedded [30]. The sampling rate is 1000 Hz, and the window length is set to be 40 ms. Due to the greater computation burden of the singular value decomposition (SVD) operation and complex matrix operation, conventional algorithms cannot complete their calculations within 1 ms in the DSP platform. Therefore, only the proposed method is evaluated with the HIL tests, where the purpose is to evaluate the its computation performance in practical engineering applications.

A real-time simulation is achieved through interaction between the Typhoon HIL and DSP controller, which is shown in Fig. 17. The wind power system under study is modeled using the Typhoon HIL hardware. The Typhoon HIL device runs the system and outputs current and voltage analog signals in real time. These current and voltage signals are fed to the DSP board in which the proposed SSCI monitoring algorithm was implemented. A flow of the proposed ITD algorithm for the DSP board is shown in Fig. 17. The DSP controller receives signals from the Typhoon HIL device using an analog-to-digital converter (ADC). The digital signal is then processed using a low-pass filter and then sent to the ITD module. In this module, the signal is first fitted using the improved ITD to obtain the frequencies of the fundamental and SSCI components. Then, the least-squares method is used to estimate the phasor of the components. Finally, the decision module determines whether oscillation occurs, and a warning signal is sent to the Typhoon HIL based on the requirements.

TABLE VI
MEAN AND VARIANCE OF RELATIVE ERRORS OF FIVE ALGORITHMS

Algorithm	Relative error (mean ± variance) (%)							
	GY-40-F	GY-40-A	GY-100-F	GY-100-A	HM-40-F	HM-40-A	HM-100-F	HM-100-A
Prony	3.28 ± 0.35	4.14 ± 4.83	0.71 ± 0.30	1.86 ± 0.05	0.88 ± 0.07	3.18 ± 0.19	0.47 ± 0.00	1.90 ± 0.11
ERA	4.07 ± 0.51	5.78 ± 6.20	0.51 ± 0.11	1.16 ± 0.03	1.02 ± 0.09	3.68 ± 0.27	0.39 ± 0.00	1.71 ± 0.07
MPM	2.48 ± 0.12	3.21 ± 4.84	0.46 ± 0.11	1.19 ± 0.03	0.87 ± 0.07	3.26 ± 0.23	0.52 ± 0.00	1.92 ± 0.07
TLS-ESPRIT	3.08 ± 0.22	4.35 ± 5.33	0.71 ± 0.11	1.67 ± 0.04	1.06 ± 0.60	3.78 ± 0.27	0.39 ± 0.00	1.71 ± 0.07
ITD	0.09 ± 0.00	1.15 ± 0.02	0.09 ± 0.00	1.15 ± 0.02	0.76 ± 0.00	1.51 ± 0.01	0.76 ± 0.00	1.51 ± 0.01

Note: GY and HM stand for Guyuan and Hami, respectively; F and A stand for frequency and amplitude, respectively; and 40 and 100 stand for 40 ms and 100 ms, respectively.

TABLE VII
TIME COMPLEXITIES OF DIFFERENT ALGORITHMS

Algorithm	Time complexity	Dominating module
ITD	$O(1061)$	Algebraic operation
Prony	$O(2772)$	Linear equations
ERA	$O(3996)$	SVD operation
Matrix pencil	$O(3996)$	SVD operation
TLS-ESPRIT	$O(3996)$	SVD operation
Bandpass digital filter-based method	$O(10^6)$	DFT operation
Improved iterative Taylor-Fourier multifrequency-model-based method	$O(5245107)$	Matrix pseudoinversion and phasor estimation

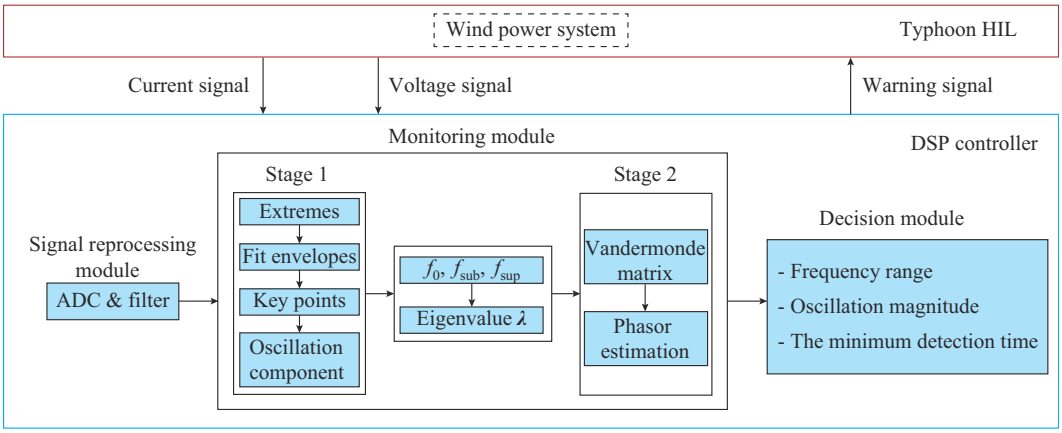

Fig. 17. Real-time simulation of Typhoon HIL and DSP controller interaction.

The total simulation time is set to be 1.5 s. At $t_1 = 0.55$ s, the series capacitor was connected to trigger SSCI. The simulation results are shown in Fig. 18(a) and (b).

As shown in Fig. 18(c) and (d), the device detects the SSCI 18 ms after its occurrence and satisfactorily tracks the frequency and amplitude when the energy of SSCI increases. Once the minimum detection time is achieved, the device sends out a warning signal at $t_3 = 0.617$ s. This shows that the proposed ITD algorithm can quickly detect the SSCI and accurately identify SSCI parameters, even in the initial stage. In addition, the algorithm is very simple and can thus be easily implemented in the hardware for real-time monitoring.

VI. CONCLUSION

In this paper, a simple and efficient algorithm is presented for rapid detection and identification of SSCI.

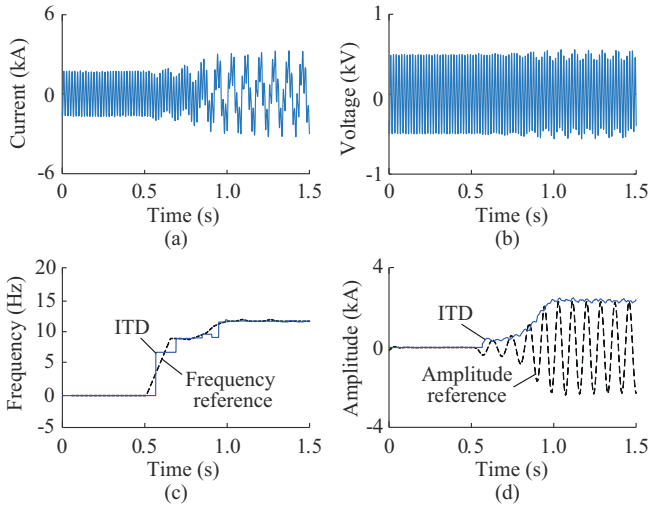

Fig. 18. HIL test results. (a) Current waveform. (b) Voltage waveform. (c) Estimated frequency. (d) Estimated amplitude.

The main purpose of this paper is to improve the ITD algorithm by incorporating the least-squares method. The main conclusions can be summarized as follows.

1) The proposed ITD algorithm combines the advantages of the original ITD algorithm and least-squares method, leading to a two-stage identification process. Results show that the proposed ITD algorithm exhibits good dynamic performance and anti-noise capability.

2) The proposed ITD algorithm is very simple and does not require any prior information. Thus, it can be easily implemented in hardware for real-time monitoring tests. A real-time simulation test is conducted, which demonstrates that the algorithm could perform well in practical engineering applications.

3) Comprehensive verification studies are conducted using synthetic signals, EMTP simulations, and field-recorded SSCI data. The results indicate that the proposed ITD algorithm is more attractive than the conventional methods that have been widely used in the industry.

APPENDIX A

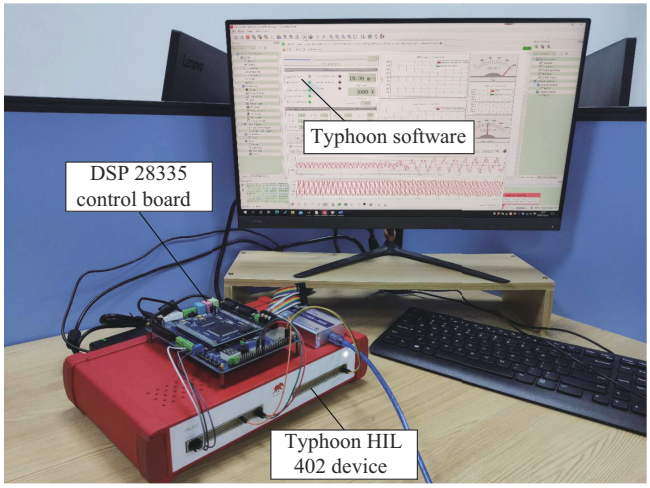

Fig. A1. Experimental platform of real-time simulation test.

REFERENCES

[1] H. L. Chi, "Simplified modelling of oscillation mode for wind power systems," *Journal of Modern Power Systems and Clean Energy*, vol. 9, no. 1, pp. 56-67, Jan. 2021.

[2] E. Pan, B. Yue, X. Li *et al*., "Integration technology and practice for long-distance offshore wind power in China," *Energy Conversion & Economics*, vol. 1, no. 1, pp. 4-19, Oct. 2020.

[3] K. Sebaa, Y. Zhou, Y. Li *et al*., "Low-frequency oscillation damping control for large-scale power system with simplified virtual synchronous machine," *Journal of Modern Power Systems and Clean Energy*, vol. 9, no. 6, pp. 1424-1435, Nov. 2021.

[4] A. S. Tummala, "A robust composite wide area control of a DFIG wind energy system for damping inter-area oscillations," *Protection and Control of Modern Power Systems*, vol. 5, no. 3, pp. 260-269, Nov. 2020.

[5] H. Liu, X. Xie, J. He *et al*., "Subsynchronous interaction between direct-drive PMSG based wind farms and weak AC networks," *IEEE Transactions on Power Systems*, vol. 32, no. 6, pp. 4708-4720, Nov. 2017.

[6] L. Zhao, Y. Zhou, I. B. M. Matsuo *et al.*, "The design of a remote online holistic monitoring system for a wind turbine," *IEEE Transactions on Industry Applications*, vol. 56, no. 1, pp. 14-21, Jan. -Feb. 2020.

[7] B. Wang, D. Yang, G. Cai *et al*., "Online inertia estimation using electromechanical oscillation modal extracted from synchronized ambient data," *Journal of Modern Power Systems and Clean Energy*, vol. 10, no. 1, pp. 241-244, Jan. 2022.

[8] A. Román-Messina, A. Castillo-Tapia, D. A. Román-García *et al*., "Distributed monitoring of power system oscillations using multiblock principal component analysis and higher-order singular value decomposition," *Journal of Modern Power Systems and Clean Energy*, vol. 10, no. 4, pp. 818-828, Jul. 2022.

[9] A. H. A. El-Kareem, M. A. Elhameed, and M. M. Elkholy, "Effective damping of local low frequency oscillations in power systems integrated with bulk PV generation," *Protection and Control of Modern Power Systems*, vol. 6, no. 4, pp. 512-524, Dec. 2021.

[10] T. Rauhala, A. M. Gole, and P. Jarventausta, "Detection of subsynchronous torsional oscillation frequencies using phasor measurement," *IEEE Transactions on Power Delivery*, vol. 31, no. 1, pp. 11-19, Feb. 2016.

[11] M. Zuhaib, M. Rihan, and M. T. A. Saeed, "A novel method for locating the source of sustained oscillation in power system using synchrophasors data," *Protection and Control of Modern Power Systems*, vol. 5, no. 4, pp. 320-331, Dec. 2020.

[12] Y. Wang, X. Jiang, X. Xie *et al.*, "Identifying sources of subsynchronous resonance using wide-area phasor measurements," *IEEE Transactions on Power Delivery*, vol. 36, no. 5, pp. 3242-3254, Oct. 2021.

[13] X. Xie, Y. Zhan, H. Liu *et al.*, "Improved synchrophasor measurement to capture sub/super-synchronous dynamics in power systems with renewable generation," *IET Renewable Power Generation*, vol. 13, no. 1, pp. 49-56, Jan. 2019.

[14] M. Netto and L. Mili, "A robust prony method for power system electromechanical modes identification," in *Proceedings of 2017 IEEE PES General Meeting*, Chicago, USA, Jul. 2017, pp. 1-5.

[15] F. Salehi, I. B. M. Matsuo, A. Brahman *et al.*, "Sub-synchronous control interaction detection: a real-time application," *IEEE Transactions on Power Delivery*, vol. 35, no. 1, pp. 106-116, Feb. 2020.

[16] J. Chen, X. Li, M. A. Mohamed *et al.*, "An adaptive matrix pencil algorithm based-wavelet soft-threshold denoising for analysis of low frequency oscillation in power systems," *IEEE Access*, vol. 8, pp. 7244-7255, Jan. 2020.

[17] S. K. Jain and S. N. Singh, "Exact model order esprit technique for harmonics and interharmonics estimation," *IEEE Transactions on Instrumentation and Measurement*, vol. 61, no. 7, pp. 1915-1923, Jul. 2012.

[18] M. Beza and M. Bongiorno, "Application of recursive least squares algorithm with variable forgetting factor for frequency component estimation in a generic input signal," *IEEE Transactions on Industry Applications*, vol. 50, no. 2, pp. 1168-1176, Apr. 2014.

[19] M. Beza and M. Bongiorno, "A modified RLS algorithm for online estimation of low-frequency oscillations in power systems," *IEEE Transactions on Power Systems*, vol. 31, no. 3, pp. 1703-1714, May 2016.

[20] T. Rajaram, J. M. Reddy, and Y. Xu, "Kalman filter based detection and mitigation of subsynchronous resonance with SSSC," *IEEE Transactions on Power Systems*, vol. 32, no. 2, pp. 1400-1409, Mar. 2017.

[21] M. Orman, P. Balcerek, and M. Orkisz, "Method of subsynchronous resonance detection," U.S. Patent 012/0303306 A1, Nov. 2012.

[22] M. Orman, P. Balcerek, and M. Orkisz, "Effective method of subsynchronous resonance detection and its limitations," *International Journal of Electrical Power & Energy Systems*, vol. 43, no. 1, pp. 915-920, Dec. 2012.

[23] B. Gao, R. Torquato, W. Xu *et al.*, "Waveform-based method for fast and accurate identification of subsynchronous resonance events," *IEEE Transactions on Power Systems*, vol. 34, no. 5, pp. 3626-3636, Sept. 2019.

[24] X. Xie, H. Liu, Y. Wang *et al*., "Measurement of sub- and supersynchronous phasors in power systems with high penetration of renewables," in *Proceedings of 2016 IEEE PES Innovative Smart Grid Technologies Conference (ISGT)*, Minneapolis, USA, Sept. 2016, pp. 1-5.

[25] L. Chen, W. Zhao, F. Wang *et al.*, "An interharmonic phasor and frequency estimator for subsynchronous oscillation identification and monitoring," *IEEE Transactions on Instrumentation and Measurement*, vol. 68, no. 6, pp. 1714-1723, Jun. 2019.

[26] M. G. Frei and I. Osorio, "Intrinsic time-scale decomposition: time-frequency-energy analysis and real-time filtering of non-stationary signals," *Proceedings of the Royal Society*, vol. 463, no. 2078, pp. 321-342, Feb. 2007.

[27] P. Tripathy, S. C. Srivastava, and S. N. Singh, "A modified TLS-ESPRIT-based method for low-frequency mode identification in power systems utilizing synchrophasor measurements," *IEEE Transactions on Power Systems*, vol. 26, no. 2, pp. 719-727, May 2011.

[28] Y. Cheng, S. H. Huang, and J. Rose, "A series capacitor based frequency scan method for SSR studies," *IEEE Transactions on Power Delivery*, vol. 34, no. 6, pp. 2135-2144, Dec. 2019.
[29] A. Gambier, "Real-time control and hardware-in-the-loop simulation for educational purposes of wind energy systems," in *Proceedings of IFAC World Congress*, Berlin, Germany, Jul. 2020, pp. 1-6.
[30] Y. Huo and G. Gruosso, "Ancillary service with grid connected PV: a real-time hardware-in-the-loop approach for evaluation of performances," *Electronics*, vol. 8, no. 7, p. 809, Jul. 2019.

Yang Wang received the B.S. degree in electrical engineering from Zhejiang University, Hangzhou, China, in 2012, and the Ph.D. degree in electrical and computer engineering from the University of Alberta, Edmonton, Canada, in 2017. From 2017 to 2018, he was a Postdoctoral Fellow with the University of Alberta. Currently, he is a Research Fellow with the College of Electrical Engineering, Sichuan University, Chengdu, China. His main research interests include power quality and integration of renewable energies.

Hanlu Yang received the B.S. degree from Southwest Jiaotong University, Chengdu, China, in 2018. He is currently working toward the M.S. degree with the College of Electrical Engineering, Sichuan University, Chengdu, China. His main research interest includes power quality.

Xiaorong Xie received the B.Sc. degree from Shanghai Jiao Tong University, Shanghai, China, in 1996, and the Ph.D. degree from Tsinghua University, Beijing, China, in 2001, where he is currently an Associate Professor with the Department of Electrical Engineering, Tsinghua University. His research interests include power system analysis and control, flexible AC transmission systems, and integration of renewable energies.

Xiaomei Yang received the Ph.D. degree from Sichuan University, Chengdu, China, in 2004, where she is currently an Associate Professor with the Department of Automation, College of Electrical Engineering. Her current research interests include power quality and data mining.

Guanrun Chen is currently working toward the B.S. degree with the College of Electrical Engineering, Sichuan University, Chengdu, China. His current research interest includes power quality.